Communication

Study of Solidification Cracking in a Transformation-Induced Plasticity-Aided Steel

G. AGARWAL, A. KUMAR, H. GAO, M. AMIRTHALINGAM, S.C. MOON, R.J. DIPPENAAR, I.M. RICHARDSON, and M.J.M. HERMANS

In situ high-temperature laser scanning confocal microscopy is applied to study solidification cracking in a TRIP steel. Solidification cracking was observed in the interdendritic region during the last stage of solidification. Atom probe tomography revealed notable enrichment of phosphorus in the last remaining liquid. Phase field simulations also confirm phosphorus enrichment leading to severe undercooling of more than 160 K in the interdendritic region. In the presence of tensile stress, an opening at the interdendritic region is difficult to fill with the remaining liquid due to low permeability and high viscosity, resulting in solidification cracking.

https://doi.org/10.1007/s11661-018-4505-7

Advanced high strength steels (AHSS) are rapidly being implemented in the automotive industry. The increased use of AHSS in car bodies is driven by both regulative guidelines and concerted effort. Transformation-induced plasticity steels (TRIP) belong to the AHSS family. These steels, with strength over 600 MPa, possess increased formability due to the TRIP effect.[1] The TRIP effect is achieved when meta-stable austenite transforms to martensite upon deformation. Matsumura[2,3] proposed the TRIP effect in low alloyed steel with a composition of C 0.2, Mn 1 to 2, and Si 1 to 2 (in wt pct). Silicon aids the TRIP effect by inhibiting cementite formation. However, an increase in the Si content beyond 0.5 wt pct reduces the galvanizability by forming silicon oxide.[4] Both Al and P are known to retard cementite formation and partially substitute Si. Phosphorus addition increases the amount of retained austenite and additions of 0.1 wt pct P stabilize small austenite grains, even at 100 K.[5] In addition, P is also an effective solution strengthening element[6,7] and addition of up to 0.25 wt pct is considered beneficial with regard to the TRIP effect. [7–9]

Apart from formability requirements in these steels, welding is an important fabrication method for automotive applications. It involves the use of an appropriate heat source to form a weld pool, which solidifies during cooling. The weld thermal cycle alters the carefully designed microstructure of the base metal in the fusion zone and in the adjacent heat-affected zone. The term weldability refers to the resistance of a material to failure during or post welding and is often used to qualitatively describe the behavior of a material subjected to welding. From the standpoint of possible welding defects,[10] preventing solidification cracking is an essential prerequisite for the safety of welded components.

Weld solidification of an alloy involves the coexistence of a solid and a liquid phase *i.e.,* a mushy zone. The mushy zone generally comprises columnar dendrites separated by liquid. Due to a temperature gradient in the mushy zone, the solid deforms due to both solidification shrinkage and non-uniform thermal contraction; as a consequence, tensile strains are induced in the semi-solid region. During the initial stage of solidification, grains are isolated and can accommodate tensile deformation by reorientation/rotation.[11] At the terminal stage of solidification, *i.e.,* when the fraction of solid (f_s) approaches 1, the grains coalesce leading to a solid network separated by isolated liquid pockets. The material at this stage possesses adequate strength and ductility and therefore has good resistance to cracking. However, prior to this stage, the grains are separated by films of the remaining liquid and hence the material possesses a low strength.[12] Any separation at the grain boundary due to thermal strain is difficult to compensate with flow of the remaining liquid owing to low permeability; this can lead to solidification cracking or hot tearing. Solidification cracking has been studied for several decades[13–18] in different alloy systems. The onset of solidification cracking involves a complex interplay between interlinked factors, namely, the solidifying microstructure, the weld thermal cycle, and the surrounding restraint. A unified model to explain the solidification cracking phenomena is still evolving.

Liquid feeding is an important factor that helps to avoid solidification cracking and likewise, is included in most of the models.[14,15,19] Early work by Feurer[19]

G. AGARWAL, A. KUMAR, H. GAO, I.M. RICHARDSON, and M.J.M. HERMANS are with the Department of Materials Science and Engineering, Faculty of 3mE, Delft University of Technology, Mekelweg 2, 2628 CD, Delft, The Netherlands. Contact e-mail: g.agarwal@tudelft.nl M. AMIRTHALINGAM is with the Department of Metallurgical and Materials Engineering, Indian Institute of Technology Madras, Chennai, 600036, India. S.C. MOON and R.J. DIPPENAAR are with the School of Mechanical, Materials and Mechatronic Engineering, Faculty of Engineering and Information Sciences, University of Wollongong, Wollongong, Australia.

Manuscript submitted November 2, 2017.
Article published online February 12, 2018

examined the rate of feeding and the rate of shrinkage effects on hot cracking phenomena. Cracking occurs during solidification, if the rate of feeding of the liquid in the interdendritic region is less than the rate of shrinkage of the solid being formed. The feeding ability is directly linked to the properties of solidifying microstructure, *e.g.,* solidification morphology, composition, and segregation of the solute.

Owing to the experimental complexity involved in studying high-temperature phenomena involving both the solid and liquid phases, most of the studies on solidification cracking are conducted *ex situ*. Externally loaded tests like the varestraint test[10] and the PVR (programmable deformation rate) test[20] focus (primarily) only on determining the critical amount of applied strain (rate) or total crack length for assessing weldability, while underlying factors such as solidifying microstructure are not considered. To address this issue, an *in situ* observation technique, namely, high-temperature laser scanning confocal microscopy, was employed in this work. This technique is generally used to study *in situ* solidification events like peritectic[21] and solid-state phase transformations; details of which can be found in the literature.[22,23]

In this work, a circular melt pool was formed at the center of a thin circular disk specimen while the outer rim remained solid. The solid outer rim acts as a restraint to the solidifying melt pool, thus allowing the simulation of welding conditions. Cracking was observed during the terminal stage of solidification. Segregation of the alloying elements phosphorus and carbon in the interdendritic region near the crack was studied using atom probe tomography (APT), which provided three-dimensional (3D) mapping of alloying elements with near-atomic resolution.[24] The results are compared with a phase field model and further discussed pertaining to the effect of P on solidification cracking.

A TRIP steel sheet with a composition, C 0.19, Mn 1.63, Al 1.1, Si 0.35, P 0.089 (all in wt pct) was examined in this study. The liquidus temperature of the steel was calculated to be 1785 K using the commercial thermodynamic software Thermo-Calc™. Circular disk specimens with a diameter of 10 mm and a thickness of 250 μm were prepared using electro-discharge machining. Further details on the heating arrangement, temperature measurements *etc.* can be found in our previous work.[23,25] A stable melt pool with a diameter between 3 and 3.5 mm was obtained at the center of the specimen while the outer rim remained solid. A cooling rate of 10 K s^{-1} was employed until 1623 K (ref. supplementary data). To obtain an approximation of the actual temperature in the liquid pool, calibration experiments with pure iron samples were conducted and a difference of 212 K was found between the thermocouple reading at the sample holder and the melting point of iron, taken as 1811 K (ref. supplementary data).

Figure 1(a) indicates the diameter of the melt pool. Figures 1(b) through (f) show the solidification sequence of the TRIP steel. A stable melt pool with a diameter of approximately 3 mm was created before the cooling cycle started, as shown in Figure 1(b). The solidification front was initially observed to be planar. However, a temperature gradient in the thickness direction of the sample led to the nucleation of dendrites from the underside of the specimen as shown in Figure 1(c). During the last stages of solidification, solidification cracking was observed *in situ* as shown in Figure 1(d). Concurrently, isolated liquid pockets could be identified at a temperature of 1615 ± 8 K (Figures 1(d) through (e)). A crack is shown clearly in Figure 1 (f) and the final extent of solidification cracking is shown in the secondary electron micrograph (Figure 1(a)).

To obtain the solute content in the last solidified liquid, three site-specific samples (S1, S2, and S3) for APT were prepared from the interdendritic region near the crack surface (Figure 2(a)) using a focused ion beam. The local elemental distribution adjacent to the crack was further investigated by APT. Figure 2(b) shows the C and P maps from one of the samples and the composition of the three interdendritic APT samples is shown in Table I. Notable enrichment of C and P was found in all three APT samples. In addition, slight enrichment in Si was also found. Silicon enrichment in the liquid can lead to the formation of a low melting point eutectic Fe-Fe_2Si (melting point = 1485 K),[26] thereby increasing the susceptibility to solidification cracking. Silicon contents above 0.65 wt pct may increase the cracking tendency in ferritic steels.[27] A secondary electron micrograph (Figure 2(c)) of the polished sample from the same region, where the APT samples were prepared, indicates the intergranular nature of solidification crack.

A multicomponent phase field model for directional solidification was constructed using MICRESS.[28,29] Two compositions were selected; one representing the TRIP steel under investigation and other with the same composition as the TRIP steel, but without P, referred to as TRIP-0P. Simulations were carried out with a grid size of 150 $\mu m \times 250$ μm and 2 μm grid resolution. The phase field code was coupled with the thermodynamic software Thermo-Calc™ to obtain equilibrium thermodynamic data. The mobility information was directly obtained from the MOB2 database of Thermo-Calc™. Four nuclei of δ ferrite were placed at the bottom of the simulation domain with an undercooling of 5 K at the underside. A cooling rate of 10 K s^{-1} and a thermal gradient of 200 K mm $^{-1}$ in the vertical direction was applied in the model, the latter based on the average solidification rate of the dendrites from the underside to the top. Energy parameters applied in the phase field model can be found in the Reference 30. To calculate the stress evolution in the solid that develops due to solidification shrinkage and thermal contraction, a fixed mechanical boundary condition (Figure 4(a)) was applied to the simulation domain. For both the steels, a constant elastic modulus of 10 GPa for the solid at high temperature[31] and 1 GPa for the liquid[32,33] was assumed. A constant thermal expansion coefficient of 2.5×10^{-5} K^{-1} and 3×10^{-5} K^{-1} was used for the solid and the liquid phases, respectively.

Figure 3(a) shows the cellular morphology of delta (δ) ferrite in the TRIP steel, growing upward from the

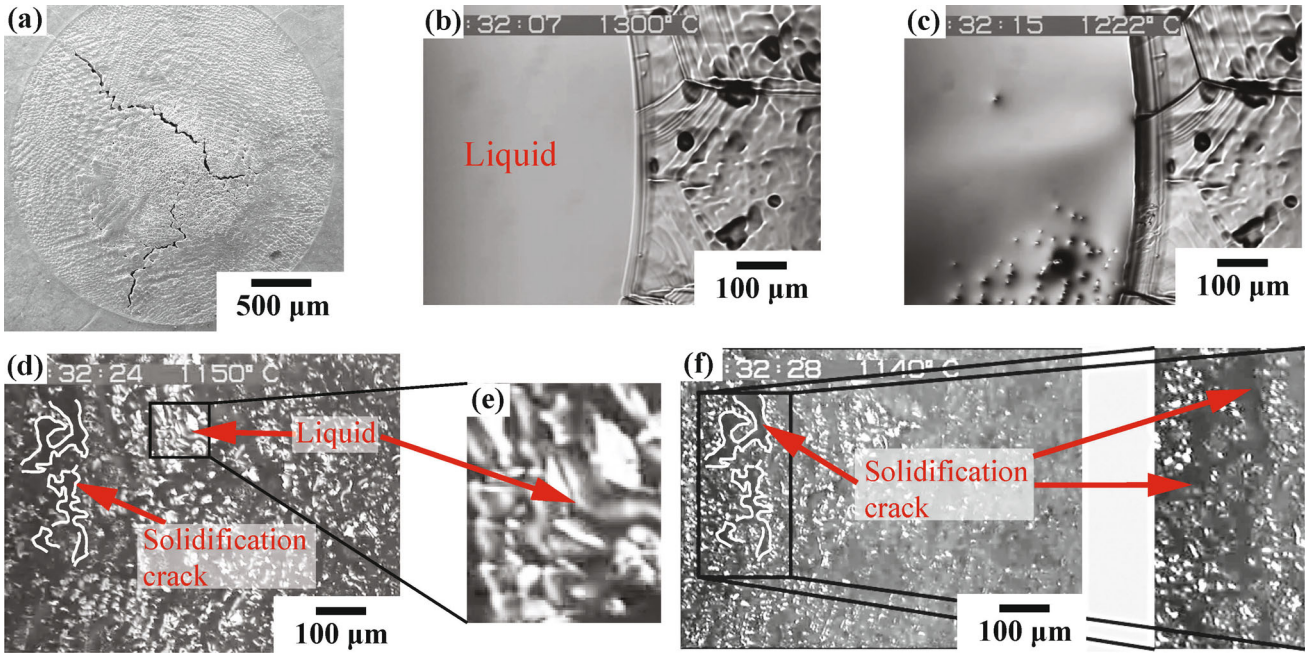

Fig. 1—(*a*) Secondary electron micrograph showing the extent of solidification cracking, (*b-f*) solidification images from the confocal microscope, (b) a stable circular melt pool of diameter ≈ 3 mm at the center of the specimen while the outer rim remains solid, (*c*) dendrites growing mostly from the bottom of the pool owing to a thermal gradient in the thickness direction, (*d-e*) solidification crack and isolated liquid pockets, (f) distinct solidification crack observed *in situ* at the last stage of solidification. Temperature indicated in images (b-d) and (f) is measured at the periphery of the platinum specimen holder. Based on calibration the actual temperature is ~ 212 K higher.

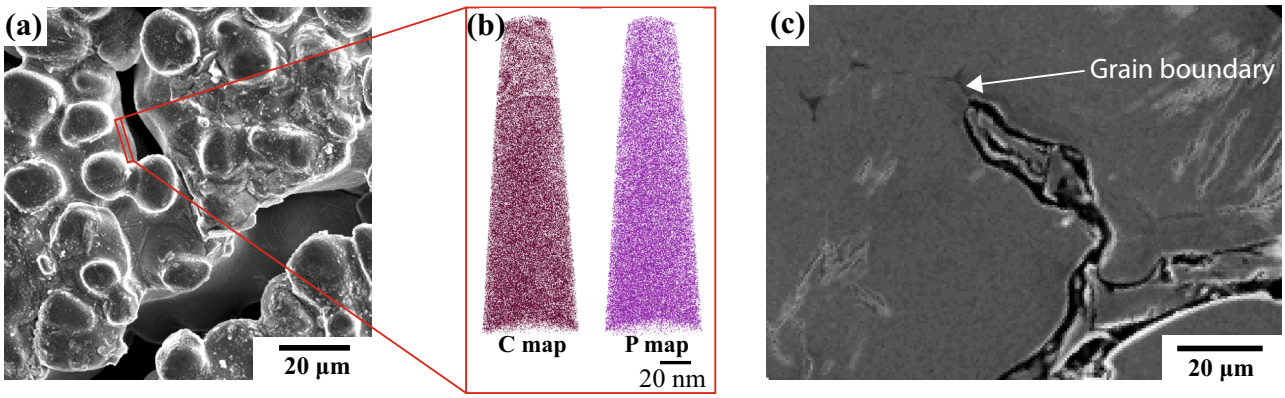

Fig. 2—(*a*) Secondary electron micrograph indicating the region from which the samples were prepared for atom probe tomography using a focused ion beam, (*b*) C and P map obtained by APT, (*c*) secondary electron micrograph (from the same region where the APT samples were prepared) indicating intergranular solidification cracking.

Table I. Bulk Composition in the Interdendritic Region of the Top Surface

	Sample			
Element (Wt Pct)	S1	S2	S3	Average
C	0.48	0.87	0.69	0.68
P	0.32	0.22	0.32	0.29
Mn	1.44	1.50	1.62	1.52
Al	0.94	0.94	1.04	0.97
Si	0.55	0.51	0.66	0.57

bottom of the domain. Carbon and phosphorus maps are shown in Figures 3(b) and (c). Due to microsegregation of C and P in the interdendritic region, the liquid in this region is undercooled. Figure 3(e) shows the temperature versus solid fraction (f_s) curves calculated from the equilibrium conditions and phase field simulations for the two steels. Experimental observation of isolated liquid pockets (Figures 1(d) through (e)) at a temperature 1615 ± 8 K (≈ 160 K undercooling) is found to be in agreement with phase field simulations, Figure 3(e). The temperature corresponds to $f_s \approx 0.99$

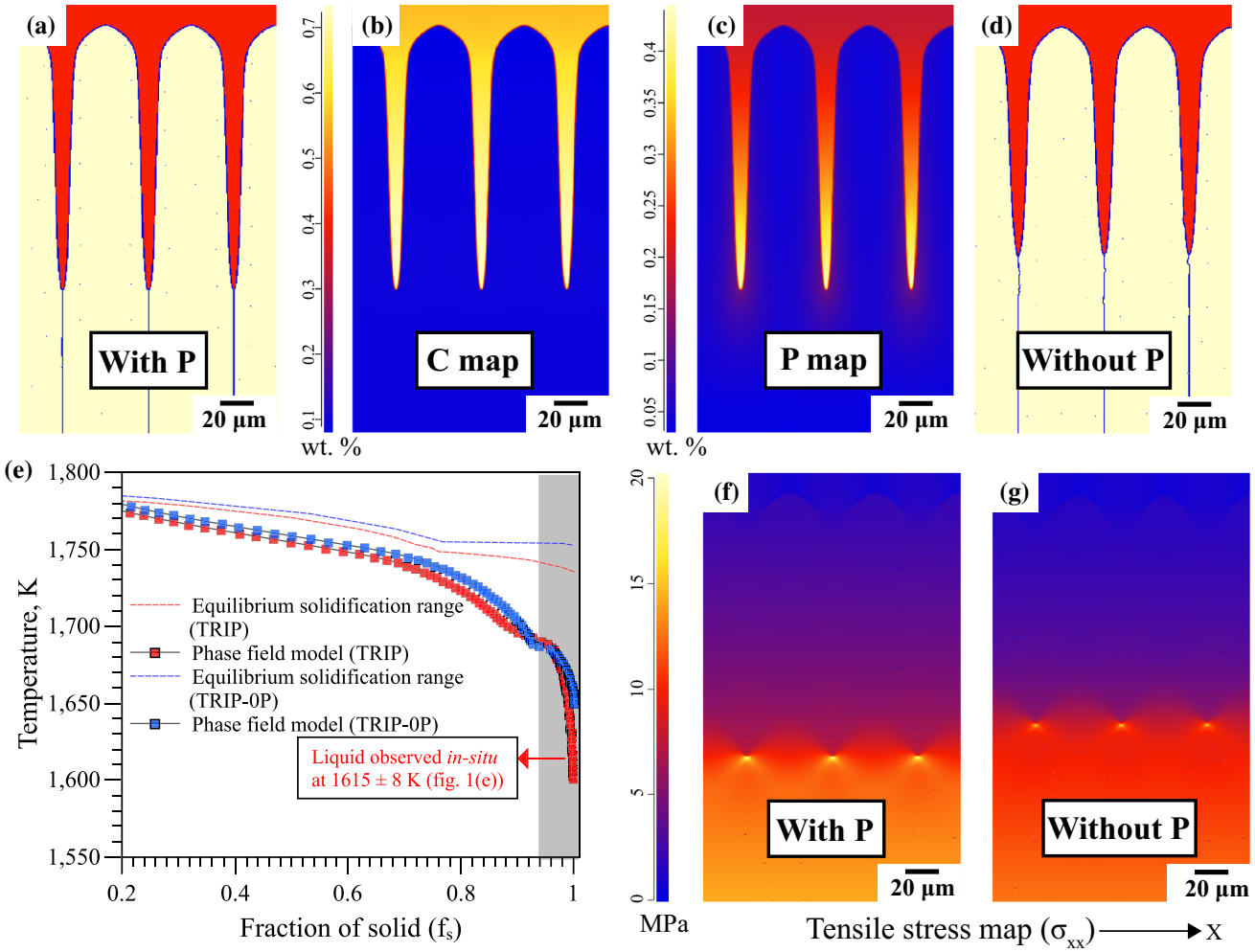

Fig. 3—Phase field simulation showing liquid channel morphology and microsegregation (*a*) TRIP steel composition, (*b*) Carbon map in TRIP steel, (*c*) Phosphorus map in TRIP steel, (*d*) phase field simulation showing liquid channel morphology for TRIP-0P steel composition, (*e*) T *vs* f_s curves for the two steels from equilibrium phase diagram and phase field simulations, (*f*) and (*g*) tensile stress map in TRIP and TRIP-0P steel, respectively.

from the phase field simulations. Due to fast solidification and limited spatial resolution, coexistence of liquid and crack prior to the image as shown in Figures 1(d) through (e) could not be verified. However, since the maximum crack width is approximately 50 μm in Figure 1(d), it can be argued that the crack must have initiated at a lower f_s. This observation is consistent with earlier studies by Rappaz *et al.*[15] and by Kou[34] in which extensive solid bridging was assumed to occur at $f_s = 0.98$ after which there is minimal susceptibility towards solidification cracking.

Figure 3(d) shows the cellular morphology of δ ferrite for the TRIP-0P steel. In comparison with the TRIP steel, the solidification rate was found to be faster in the TRIP-0P steel. For the sake of the ensuing discussion, the same liquid fraction ($f_L = 0.13$) is shown in both cases, where the temperature of the TRIP steel is 10 K lower than that of the TRIP-0P steel. Any opening at the interdendritic boundary due to tensile stress needs to be compensated by liquid feeding. Liquid flow in a porous medium is related to the pressure gradient as described by Darcy's law,[35,36]

$$v_l f_L = -\frac{K}{\eta}\left[\frac{\Delta P}{Z} + \rho g_z\right], \qquad [1]$$

where v_l is the interdendritic velocity of the liquid; f_L is the fraction of liquid; K is the permeability in the mushy zone; η is the viscosity of the liquid; ΔP is the pressure difference between the tip and root of the dendrite and Z is the length of the liquid channel. The prevailing conditions are described in the schematic Figure 4(a). In comparison, longer and narrower liquid channels exist in the TRIP steel (Figure 3(a)) than in the TRIP-0P steel (Figure 3(d)). Considering Darcy's law [1], a higher feeding rate v_l is required in the TRIP steel in order to avoid cracking for a similar pressure difference. In addition, the effect of η should also be considered. Viscosity is an important parameter that leads to the kinetic slowdown of a melt being undercooled due to solute enrichment.[37] The generalized form of the viscosity of a liquid alloy as a function of temperature follows an Arrhenius curve.[38] Therefore, η

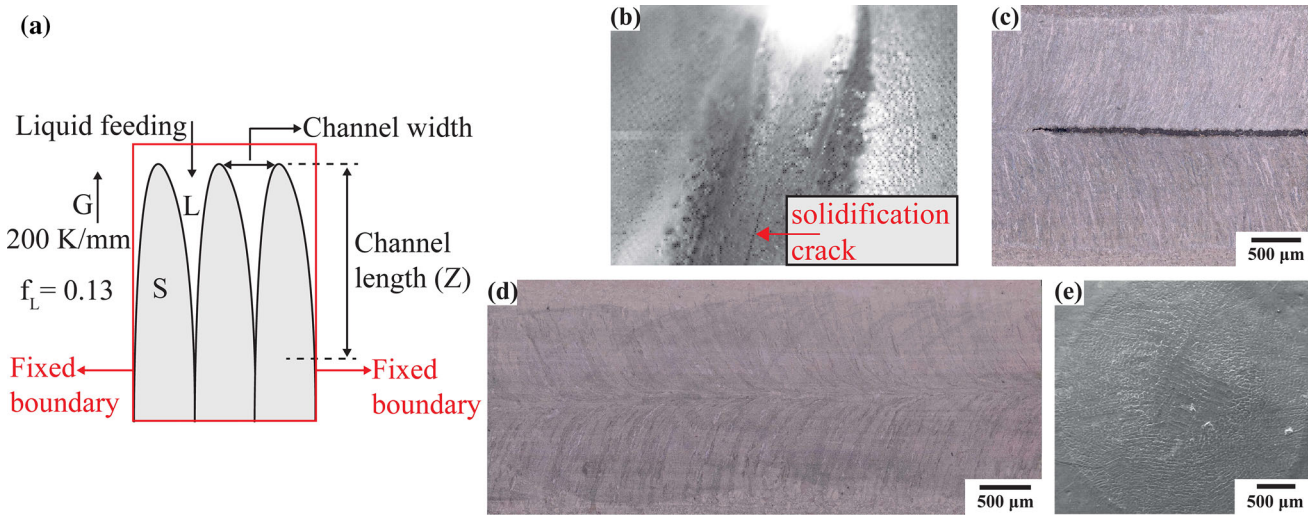

Fig. 4—(*a*) Schematic illustrating the solidifying morphology and boundary conditions. Please refer to Fig. 1(c), (*b*) high-speed camera image taken during welding of TRIP steel showing solidification cracking, (*c*) optical macrograph of the weld surface of TRIP steel, (*d*) optical macrograph of the weld surface of the steel with 0.01 wt pct P, (*e*) secondary electron image of the steel with 0.01 wt pct P after melt pool solidification.

in the interdendritic region increases as the extent of undercooling increases, further increasing the barrier for adequate liquid feeding. Note that, liquid flow was not considered in the present phase field model and therefore only relative liquid feeding capability is discussed.

Figures 3(f), (g) shows the map of tensile stress (σ_{xx}) in TRIP and TRIP-0P steel, respectively. Due to the solidification morphology (longer dendrite arms) and the greater thermal contraction at the root of the dendrites, associated with the 10 K lower temperature, the TRIP steel exhibits a higher tensile stress ($\approx 19\,MPa$) concentration at the dendritic boundaries close to the root compared to $\approx 15\,MPa$ for the TRIP-0P steel. There is negligible stress in the arms of the dendrites due to the presence of liquid in between, *i.e.,* coalescence has not occurred. The higher magnitude of tensile stress in TRIP steel increases the susceptibility to form a solidification crack. Next, the factors that lead to an opening near the root of the dendrites are considered. The opening occurs in the form of microvoids due to thermally induced stress.[13] These voids are generally nucleated at grain boundaries since these provide an existing surface and thereby contribute to the driving force. Phosphorus segregation at the grain boundaries is known to promote decohesion.[39–41] The average phosphorus concentration in TRIP steel from the three samples taken near the crack was measured to be 0.29 wt pct, *i.e.,* more than three times the nominal composition. When compared to TRIP-0P, a lower critical stress at the grain boundary in TRIP steel will lead to an opening at the grain boundary.

Two associated phenomena related to P increase the solidification cracking susceptibility. Firstly, microsegregation of P leads to severe undercooling in the interdendritic region making the liquid channels longer and narrower. Secondly, phosphorus segregation at the grain boundary promotes decohesion, *i.e.,* a solidification crack can nucleate at a lower thermally induced critical tensile stress. An opening thus formed is relatively difficult to fill with the remaining liquid due to low permeability and high viscosity, eventually leading to cracking.

In order to test the premise of confocal microscopy results, autogenous or melt-run welding experiments were conducted under identical conditions using a Nd:YAG laser. TRIP steel sheets and steel sheets with low P (0.01 wt pct) were selected. Figure 4(b) shows a high-speed camera image taken during welding of the TRIP steel. A solidification crack was observed to follow the trailing edge of the weld pool. Figure 4(c) shows the macrostructure of the weld surface indicating the centerline crack. In the steel with 0.01 wt pct P, solidification cracking was not observed in either the laser welding (Figure 4(d)) or the confocal microscopy experiments (Figure 4(e)). Consistent results from the two experimental methods thus show that the TRIP steel with 0.089 wt pct P is prone to cracking during solidification under welding conditions. It is thus emphasized that a sufficiently low amount of P is needed to achieve good weldability, without compromising its role in the TRIP effect.

In summary, solidification of a TRIP steel with 0.089 wt pct P was studied and solidification cracking was observed in the final stages of solidification. Microsegregation of P leads to undercooling resulting in longer and narrower liquid channels that persist in the crack vulnerable region. In addition, P segregation renders the grain boundaries weak. As a result, tensile strain/stress are concentrated at the interdendritic boundaries leading to increased susceptibility towards cracking. Conversely, lack of P in the TRIP steel leads to shorter and wider liquid channels that can be fed relatively easily in the event of an opening at the root of the solidifying

dendrites. In a steel with a small amount of P (0.01 wt pct) no solidification cracking was observed.

This research was carried out under project numbers F22.8.13485a and F22.8.13485b in the framework of the Partnership Program of the Materials innovation institute M2i (https://www.m2i.nl) and the Foundation for Fundamental Research on Matter (FOM) (https://www.fom.nl), which is part of the Netherlands Organisation for Scientific Research (https://www.nwo.nl). The authors would like to thank the industrial partner in this project 'Tata Steel Nederland B.V.' for its financial support.

OPEN ACCESS

ELECTRONIC SUPPLEMENTARY MATERIAL

The online version of this article (https://doi.org/10.1007/s11661-018-4505-7) contains supplementary material, which is available to authorized users.

REFERENCES

1. T. Senuma: *ISIJ Int*., 2001, vol. 41 (6), pp. 520–32.
2. O. Matsumura, Y. Sakuma, and H. Takechi: *Trans. ISIJ*, 1987a, vol. 27a(7), pp. 570–79.
3. O. Matsumura, Y. Sakuma, and H. Takechi: *Scr. Metall*., 1987b, vol. 21b(10), pp. 1301–06.
4. J. Mahieu, J. Maki, B. De Cooman, and S. Claessens: *Metall. Mater. Trans. A*, 2002, vol. 33A, pp. 2573–80.
5. E. Jimenez-Melero, N. van Dijk, L. Zhao, J. Sietsma, S. Offerman, J. Wright, and S. van der Zwaag: *Acta Mater*., 2009, vol. 57 (2), pp. 533–43.
6. H.C. Chen, H. Era, and M. Shimizu: *Metall. Trans. A*, 1989, vol. 20A, pp. 437–45.
7. B.D. Cooman: *Curr. Opin. Solid State Mater. Sci*., 2004, vol. 8 (3), pp. 285–303.
8. H.K.D.H. Bhadeshia and D.-W. Suh: *Ironmak. Steelmak*., 2015, vol. 42 (4), pp. 259–67.
9. J. Wang and S. V. D. Zwaag: *Z. Metallkd*., 2001, vol. 92(12), pp. 1299–1305.
10. J. Lippold: *Welding Metallurgy and Weldability*, 1st ed., Wiley, New York, 2014, pp. 1–400.
11. W. Mirihanage, M.D. Michiel, A. Reiten, L. Arnberg H. Dong, and R. Mathiesen: *Acta Mater*., 2014, vol. 68, pp. 159–68.
12. M. Rappaz and J. Dantzig: *Solidification*, 1st ed., EFPL Press, Lausanne, 2009, pp. 538–42.
13. L. Aucott, D. Huang, H. Dong, S. Wen, J. Marsden, A. Rack, and A. Cocks: *Sci. Rep*., 2017, vol. 7, p. 40255.
14. S. Kou: *Acta Mater*., 2015, vol. 88, pp. 366–74.
15. M. Rappaz, J.M. Drezet, and M. Gremaud: *Metall. Mater. Trans. A*, 1999, vol. 30A, pp. 449–55.
16. W.S. Pellini: *Foundry*, 1952, vol. 80, pp. 124–33.
17. N.N. Prokhorov: *Svar Proiz*, 1956, vol. 6, pp. 5–11.
18. I. Medovar: *Avtomatich. Svarka*, 1954, vol. 7, pp. 12–28.
19. U. Feurer: *Proceedings of the International Symposium on Engineering Alloys*, Delft, pp. 131–145.
20. T. Kannengießer and T. Böllinghaus: *Weld. World*, 2014, vol. 58 (3), pp. 397–421.
21. S. Griesser, C. Bernhard, and R. Dippenaar: *Acta Mater*., 2014, vol. 81, pp. 111–20.
22. H. Shibata, Y. Arai, M. Suzuki, and T. Emi: *Metall. Mater. Trans. B*, 2000, vol. 31B, pp. 981–91.
23. M. Reid, D. Phelan, and R. Dippenaar: *ISIJ Int*., 2004, vol. 44 (3), pp. 565–72.
24. Y-S. Chen, D. Haley, S.S.A. Gerstl, A.J. London, F. Sweeney, R.A. Wepf, W.M. Rainforth, P.A.J. Bagot, and M.P. Moody: *Science*, 2017, vol. 355 (6330), pp. 1196–99.
25. S. Griesser and R. Dippenaar: *ISIJ Int*., 2014, vol. 54 (3), pp. 533–35.
26. V. Shankar, T.P.S. Gill, S.L. Mannan, and S. Sundaresan: *Sadhana*, 2003, vol. 28 (3), pp. 359–82.
27. N. Bailey: *Weldability of Ferritic Steels*, 1st ed., Woodhead Publishing, Sawston, 1994, pp. 69–70.
28. https://www.micress.de.
29. I. Steinbach and F. Pezzolla: *Physica D*, 1999, vol. 134 (4), pp. 385–93.
30. M. Amirthalingam, E.M. van der Aa, C. Kwakernaak, M.J.M. Hermans, and I.M. Richardson: *Weld. World*, 2015, vol. 59 (5), pp. 743–55.
31. W.-Y. Wang, B. Liu, and V. Kodur: *J. Mater. Civ. Eng*., 2013, vol. 25 (2), pp. 174–82.
32. N. Coniglio and C. Cross: *Metall. Mater. Trans. A*, 2009, vol. 40 (11), pp. 2718–28.
33. C. Bordreuil and A. Niel: *Comput. Mater. Sci*., 2014, vol. 82 (Supplement C), pp. 442–50.
34. S. Kou: *Weld. J*., 2015, vol. 94 (12), pp. 374s–88s.
35. K. Kubo and RD. Pehlke: *Metall. Trans. B*, 1985, vol. 16B, pp. 359–66.
36. D.R. Poirier: *Metall. Trans. B*, 1987, vol. 18B, pp. 245–55.
37. Z. Evenson, S. Raedersdorf, I. Gallino, and R. Busch: *Scripta Mater*., 2010, vol. 63 (6), pp. 573–76.
38. R.N. Singh and F. Sommer: *Mon. Chem*., 2012, vol. 143 (9), pp. 1235–42.
39. R. Wu, A.J. Freeman, and G.B. Olson: *Science*, 1994, vol. 265 (5170), pp. 376–80.
40. F. Christien, R.L. Gall, and G. Saindrenan: *Scripta Mater*., 2003, vol. 48 (1), pp. 11–16.
41. C. Naudin, J. Frund, and A. Pineau: *Scripta Mater*., 1999, vol. 40 (9), pp. 1013–19.